

An Inverse Design Wavelength Demultiplexer for On-Chip Photoluminescence Sorting in TMDC Heterostructures

Anastasiia Zalogina^{1,2,*}, Chi Li^{3,*}, Ivan Zhigulin¹, Nathan Coste^{1,2}, Hossein Alijani^{1,2}, Otto Cranwell Schaeper^{1,2}, Hugo Charlton^{1,2}, Joseph Ward³, Haoran Ren^{3,*}, Igor Aharonovich^{1,2}

¹ School of Mathematical and Physical Sciences, University of Technology Sydney, Ultimo, New South Wales 2007, Australia

² ARC Centre of Excellence for Transformative Meta-Optical Systems, University of Technology Sydney, Ultimo, New South Wales 2007, Australia

³ School of Physics and Astronomy, Faculty of Science, Monash University, Melbourne, Victoria 3800, Australia

* Corresponding authors: anastasiia.zalogina@uts.edu.au, chi.li1@monash.edu, haoran.ren@monash.edu

Abstract

Emerging two-dimensional transition metal dichalcogenides (TMDCs) offer a promising platform for on-chip integrated photonics because of their unique optical and electronic properties. Their naturally passivated surfaces make them highly tolerant to lattice mismatch, enabling seamless heterogeneous integration by stacking different van der Waals materials, a crucial step in the development of advanced photonic devices. Here, we demonstrate the use of an inverse design wavelength demultiplexing waveguides for on-chip sorting and routing of distinct photoluminescence from the heterojunction formed by WS₂ and WSe₂ monolayers. The integrated nanophotonic chip splits and sorts excitonic emission into individual waveguides at room temperature. Our demonstration opens up new perspectives for integrating light sources in van der Waals materials with functional integrated photonics, offering a versatile platform for both fundamental research and practical applications.

Recent advances in integrating van der Waals (vdW) materials into photonic architectures have demonstrated their potential to enhance system scalability and performance [1-4]. These improvements stem from their novel optical properties and weak out-of-plane dangling bonds, which facilitate seamless integration onto chips. Compared to conventional semiconductors, vdW materials offer precise control over layer thickness and enable heterostructure stacking, making them ideal candidates for on-chip integration. A monolayer of transition metal dichalcogenides (TMDCs) is particularly attractive due to its exceptional electronic and optical properties [5-7]. Beyond their attractive electronic properties, TMDCs exhibit rich optical characteristics originating from excitonic photoluminescence (PL), which holds promise for photonic applications and provide a platform for exploring exciton physics relevant to spintronics and valleytronics [8-13].

Incorporating vdW materials into photonic devices allows the use of excitons for light-emitting applications, including examples of MoTe₂-based light-emitting diodes and photodetectors [14], field-effect transistors [15], and interlayer exciton emissions in MoSe₂/WSe₂ heterostructures for valley routing [16] and lasing [17]. Furthermore, recent advances in computational inverse design have begun to reshape the landscape of structures available to nanophotonics. Unlike traditional photonic design, which is usually based on intuitive rescaling or template reuse, inverse design employs optimization algorithms to discover optical structures based on desired functional characteristics with maximized performance [18-21].

Here, we demonstrate the use of an inverse design wavelength demultiplexer for on-chip sorting and guiding of PL from stacked WS₂ and WSe₂ monolayers. Our nanophotonic chip is designed to efficiently sort and separate excitonic PL from WS₂, WSe₂, and interlayer excitons into three distinct waveguide channels. Figure 1 schematically illustrates the functional nanophotonic device. A heterostructure formed by stacking monolayers of WS₂ and WSe₂ functions as the light source of the device. This heterostructure has different band gaps and work functions of the two monolayers, resulting in a type-II band alignment. In this configuration, the conduction band minimum and valence band maximum are spatially separated in adjacent layers, allowing the formation of an interlayer exciton through the Coulomb interaction between electrons and holes confined to different monolayers [22-25]. These excitonic emissions are subsequently coupled into waveguide modes that are highly confined along the waveguide.

To enhance the coupling efficiency, we added grating-based in- and out-couplers at the ends that enable efficient incoupling of exciton PL into the waveguide, as well as outcoupling of the sorted emission to the far-field for optical detection. The exciton PL at three different wavelengths, at ~620 nm from the WS₂ exciton, ~750 nm from the WSe₂ exciton, and ~870 nm from the interlayer exciton, is guided to the inverse-design wavelength demultiplexer, which splits the PL into three separate outputs (see Figure 1). Our design is not limited to TMDCs but can be adapted for any optically active layered materials, offering a versatile platform for next-generation on-chip photonics.

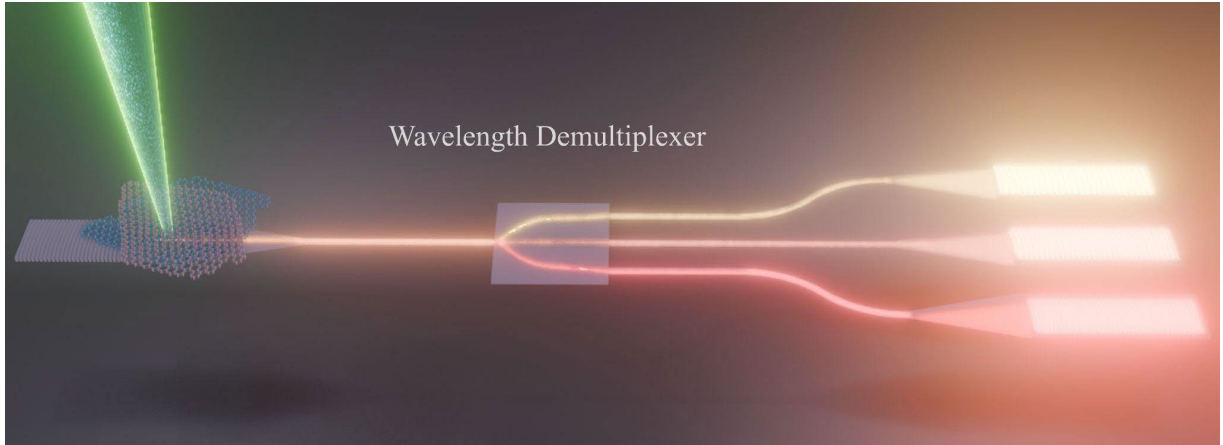


Figure 1. Schematic of the nanophotonic chip based on a TMDCs heterostructure and an inverse design wavelength demultiplexer for on-chip sorting excitonic PL. The heterostructure of the TMDCs consists of WS_2 and WSe_2 monolayers stacked together and placed on a grating in-coupler. The distinct PL of the WS_2 , WSe_2 , and interlayer excitons is guided into the wavelength demultiplexer, which splits the emission into three outputs.

We employ a gradient-based optimization approach for the demultiplexer design to sort the three excitonic emissions [19, 26-29]. As shown in Figure 2(a), the demultiplexer consists of low-loss silicon nitride (Si_3N_4) on top of a quartz substrate. To support broader spectral range, the waveguide dimensions (400-nm width and 314-nm height) of the input and output channels were selected to support the fundamental transverse electric (TE) mode. An example TE mode profile is shown in the inset, where the electric field along the Y direction is seen to be largely confined within the Si_3N_4 structure. The corresponding effective mode indices for 620 nm, 750 nm and 870 nm are 1.76, 1.66 and 1.56 respectively. For comparison, fundamental transverse magnetic (TM) modes show a slightly lower effective index where the electric field aligns with the Z axis (see Figure S1 in Supplementary Information). To simplify, in the following optimization processes, we considered only the TE mode as the excitation source. Importantly, due to the small index difference, the TM mode was also confirmed to work for the optimized structure (see Figure S2 in the Supplementary Information).

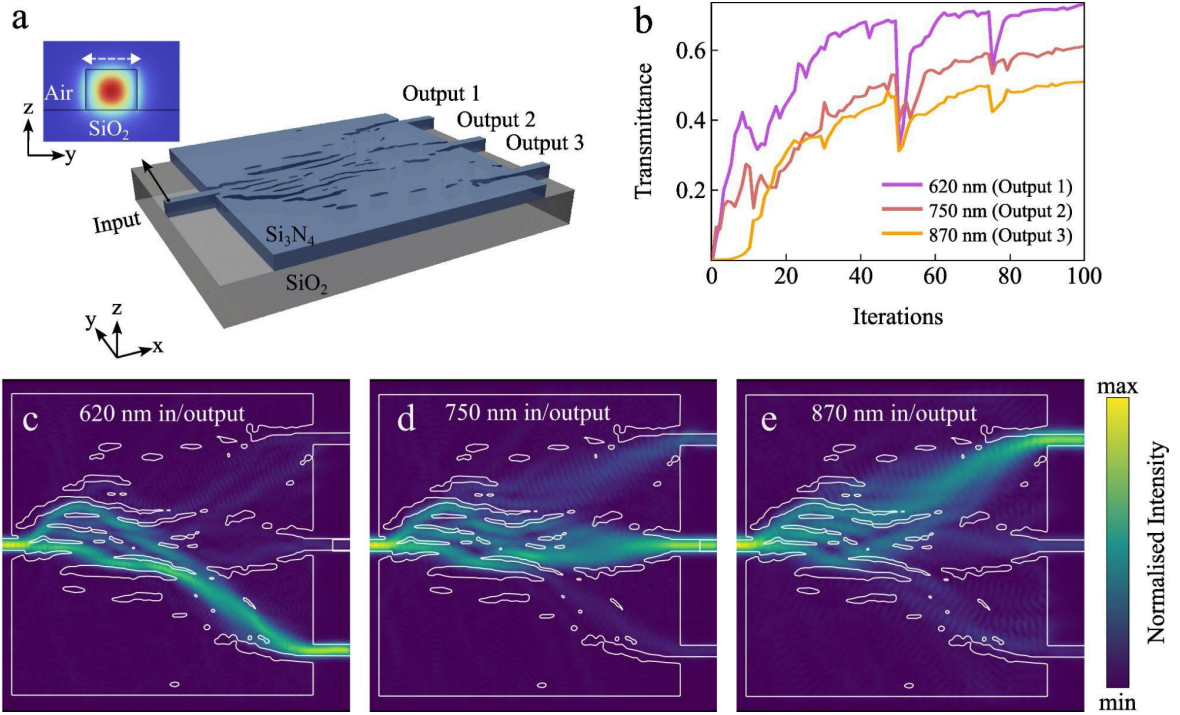


Figure 2. Numerical simulations and design. (a) Demultiplexer configuration: a thin layer of Si_3N_4 on a quartz substrate with one input, a square demultiplexer region, and three patterned output channels. Inset: a fundamental TE waveguide mode confined in the input waveguide, the dashed arrow marks its polarisation orientation. (b) Transmittance evolution for the three output channels. Electric field magnitude distribution of the demultiplexer at input of 620 nm (c), 750 nm (d), and 870 nm (e) after 100 iterations.

The photonic problem starts with the optimization goal which is defined by an objective function, f_{obj} . The inverse-design wavelength demultiplexer uses an optimization algorithm to minimize this function for topology optimization. The process can be described as: $\min_p f_{obj}(E(\epsilon(p)))$, where p is a parameterization vector that is possible to practically fabricate any target device, ϵ is the permittivity distribution, E is the electric field distribution in three dimensions, and f_{obj} is the objective function for global optimization. In short, optimizing the entire device performance means minimizing the objective function, which can be calculated based on an electromagnetic field simulation solver [19]. We define the objective function as $f_{obj}=(1-T_{620})^2+(1-T_{750})^2+(1-T_{870})^2$, where T_{620} , T_{750} , and T_{870} are the transmittance at the corresponding output channels, which are shown in Figure 2(b) as the output transmittance versus the iteration number.

The inverse design program uses adjoint finite-difference frequency domain (FDFD) simulations to iteratively optimize the output powers of target modes, with the transmittance stabilizing after approximately 80 iterations, reaching final values of 74%, 60%, and 53% for the respective channels. To ensure fabrication compatibility, a minimum feature size of 60 nm was applied, and the optimization was validated using COMSOL simulations, showing

consistent results despite slight transmittance variations due to binarization in the final discretization step (see more details in the Supplementary Information).

The device fabrication was done using electron beam lithography and pattern transfer with plasma etching (see details in Methods, Figure S3). Figure 3(a) shows a scanning electron microscope image (SEM) of the fabricated device.

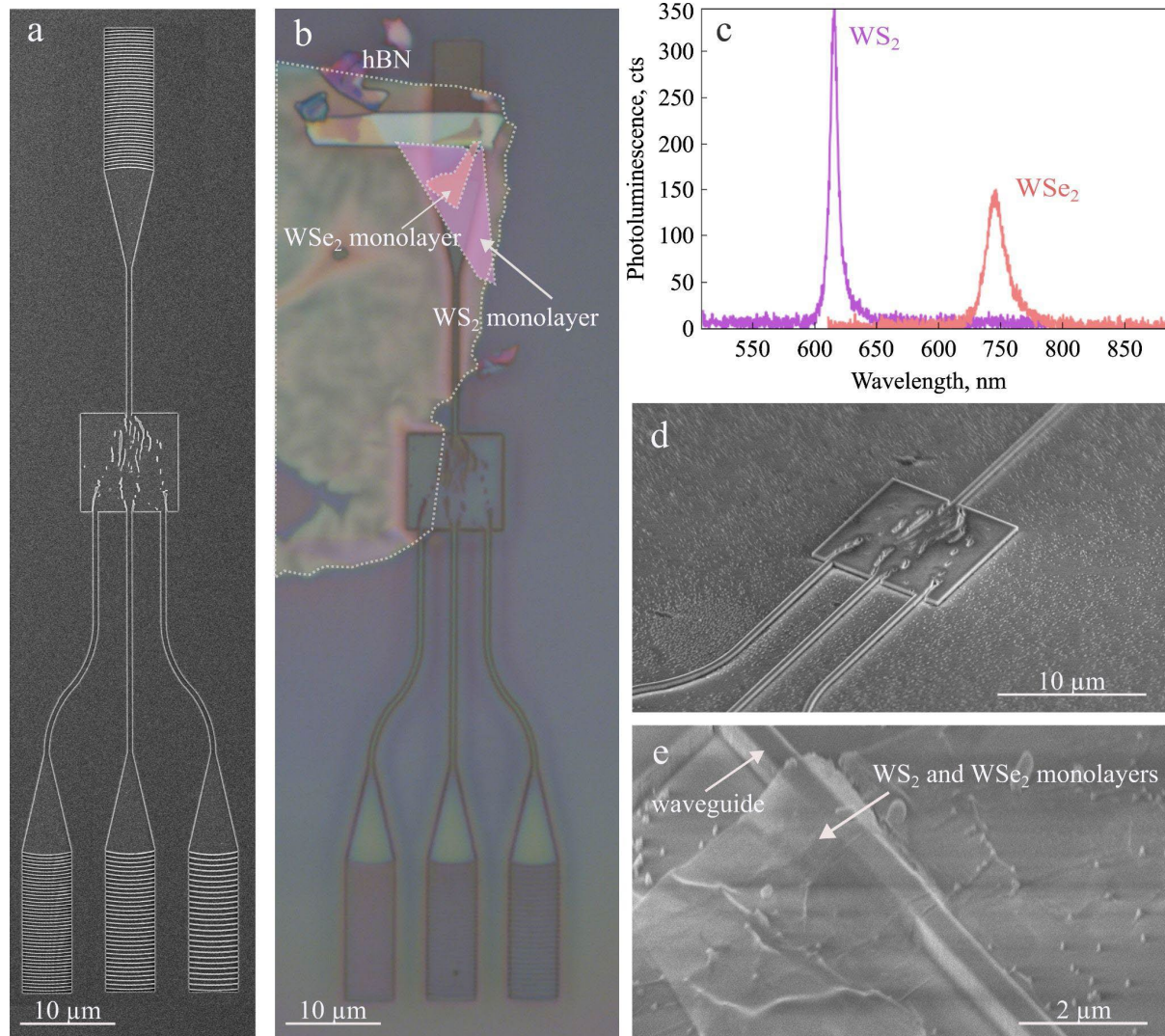


Figure 3. Device fabrication and transfer. (a) Top-view scanning electron microscope (SEM) image of the fabricated device. (b) Optical microscope image of WS₂/WSe₂ heterostructure on the fabricated device. The monolayers WS₂ and WSe₂ are indicated in pink and orange, respectively, while the hBN layer is shown in an uncolored dashed area. (c) Photoluminescence (PL) of the monolayers before their transfer onto the device. The peak wavelengths are 615 nm for WS₂ and 745 nm for WSe₂. (d) SEM image of the fabricated device tilted at 52 degrees. (e) SEM image of the monolayers placed on top of the device, showing deformation of the monolayers' shape.

To prepare a WS₂/WSe₂ heterostructure, monolayers were mechanically exfoliated from bulk WS₂ and WSe₂ crystals, respectively. Exfoliating TMDCs down to monolayers allows their

bandgaps to become direct for strong exciton emission [30, 31]. The monolayers were identified and selected using a combination of optical contrast and PL measurements (see Figure 3(c)), where peaks at 615 and 745 nm correspond to exciton emission in the WS₂ and WSe₂ monolayers, respectively. Using the dry transfer technique, the monolayers were transferred and stacked with a polydimethylsiloxane (PDMS) stamp. The WS₂ and WSe₂ monolayers are shown in pink and orange in Figure 3(b). The stack is encapsulated with hexagonal boron nitride (hBN) to protect it from the environment and prevent natural oxidation (dashed line in Figure 3(b)).

Achieving precise alignment with the device and placing the monolayers onto it is crucial. This was achieved from a home-built set-up that includes an optical microscope and micromanipulators (see Methods for details). TMDC flakes were transferred directly onto the surface of PDMS by mechanical exfoliation of the bulk material with tape. As the stamp and glass slide are transparent, the vdW flakes can be precisely aligned on the target substrate using the microscope and micromanipulators. Finally, the stamp is slowly peeled off to form a heterostructure.

PL spectra were checked again after the transfer of WS₂/WSe₂ heterostructure (see Figure S4(a) in Supplementary Information). However, we did not observe an interlayer exciton PL at 870 nm from our heterostructure, possibly due to environmental interference or the introduction of defects during the transfer process. Placing monolayers on the structures may cause slight bending, introducing strain (see Figure 3(d)) that could prohibit interlayer excitons by creating competition between interlayer coupling and band structure modulation effects [32, 33]. Additionally, defects in the monolayers can create nonradiative recombination pathways, where the PL emission of interlayer excitons is buried under a broadened, defect-bound emission background.

Transmission measurements of the pristine fabricated device (that is, before transferring the heterostructure) are shown in Figure 4(a-c). The device was characterized with laser light directed into the in-coupler at the designed wavelengths corresponding to the TMDC excitons and the interlayer exciton: 620 nm, 750 nm, and 870 nm (Figures 4 (a), (b), and (c), respectively). The collected signal from the out-couplers, measured with an avalanche photodiode (APD), is presented and overlaid with SEM images for reference.

As observed in Figure 4(a), most of the 620 nm light is guided into the designed output 1, although some light leaks into output 2. Figure S4(b) in the Supplementary Information shows that 69.7% of 620 nm emission is guided into output 1, 20.5% into output 2, and 9.8% into output 3. The 750-nm and 870-nm light were better sorted, as can be seen visually in Figure 4(b) and 4(c), respectively. From the 750-nm PL emission, 6.2% is guided into output 1, 83.7% into output 2, and 10.1% into output 3. And finally, for 870 nm, emission of 1.3% is guided to output 1, 11% to output 2, and 87.8% to output 3. These trends align with the data extracted from numerical simulations, which are overlaid with the experimental data in Table 1. In general, the device sorts the light according to the simulated design, including demultiplexing crosstalk that occurs between the channels. The crosstalk likely originates from the final pattern binarization and difference in the mesh resolution between the FDFD solver and COMSOL,

compounded by fabrication imperfections observed in the experimental measurements (see Section S2 in the Supplementary Information).

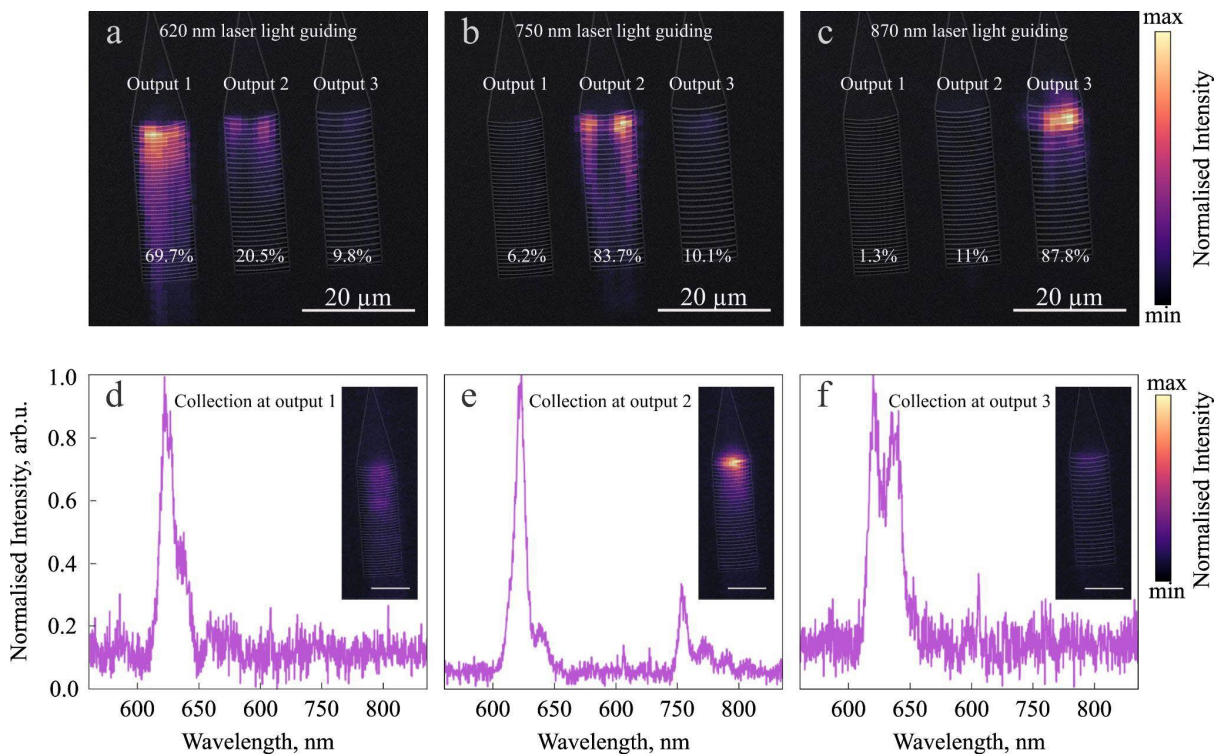


Figure 4. Optical measurements. (a-c) Wavelength sorting with a laser before transferring the monolayers: normalized PL intensities detected using avalanche photodiodes, overlaid with SEM images for guidance. The device light guiding was tested with laser light at wavelengths and powers of 620 nm and 0.08 mW (a), 750 nm and 0.08 mW (b) and 870 nm and 6 mW (c). (d-f) PL spectra measured after transferring the monolayers, excited at a wavelength of 532 nm. The insets show normalized PL intensities overlaid with SEM images, corresponding to output 1 in (d), output 2 in (e), and output 3 in (f). The scale bars in the insets are 10 μm .

Next, we characterise the device with the transferred WS_2/WSe_2 heterostructure. The monolayers were excited with a 532 nm laser (from top, directly at the heterostructure), and the emission was collected through the out-couplers. Figure 4 (d-f) shows the obtained spectra. The results demonstrate overall transmission from both monolayers, consistent with the laser characterization. The WS_2 exciton emission guide exhibits higher efficiency, likely due to its being a brighter exciton of the two monolayers (as shown in Figure 3). Additionally, the apparent stronger signal from the second output can be explained by a better directionality of this out-coupler, as seen in the insets, which facilitates a better spectrum acquisition. These results demonstrate the successful implementation of an on-chip demultiplexer and its utility to filter and guide excitonic emission.

Table 1. Contrast ratios corresponding to experimental measurements and numerical simulations that were extracted from Figure 4(a-c) and Figure S2, respectively.

	Output 1			Output 2			Output 3		
	Experiment	Theory (TE)	Theory (TM)	Experiment	Theory (TE)	Theory (TM)	Experiment	Theory (TE)	Theory (TM)
620 nm	69.7%	95.9%	84.6%	20.5%	0.9%	0.7%	9.8%	3.3%	8.4%
750 nm	6.2%	20.8%	2.6%	83.7%	74.5%	92.8%	10.1%	4.7%	4.6%
870 nm	1.3%	2.9%	6.9%	11.0%	37.5%	12.0%	87.8%	59.6%	81.2%

In conclusion, we have demonstrated the integration of WS₂/WSe₂ heterostructures with an inverse-designed photonic demultiplexer, achieving wavelength-selective routing of exciton PL at room temperature. The advanced capabilities of the inverse design were validated by testing the fabricated device with laser excitation that aligns closely with numerical simulations. Using such an inverse-designed fabricated device, we successfully guided WS₂ and WSe₂ exciton emissions into different channels. Although interlayer exciton PL was not observed, likely because of strain and environmental interference, our approach highlights the potential of combining van der Waals materials with nanophotonic devices, which represents a significant step toward the development of fully integrated van der Waals photonic systems.

Methods

Numerical Simulations. In the demultiplexer optimization, the waveguide width was set to 400 nm, while the demultiplexer was a 10- μ m square region. A constant refractive index of 2.02 was used for all three wavelengths. Port/channel transmittances are calculated by square the mode overlap that is the ratio between output and input waveguide mode. The Python-based inverse design program was built on an open-source simulation framework named SPINS-B, shared by Stanford University. Electromagnetic field simulations were conducted using its built-in FDFD solver. To save computation time, we used a homogeneous mesh size of 50 nm for the 3D simulation. The optimization program was run on a high-performance laptop

workstation equipped with an A1000 GPU and 20 GB of GPU memory. The optimized structure was further verified using COMSOL Multiphysics prior to nanofabrication.

Fabrication. To fabricate demultiplexers with waveguides, a 1000-nm SiO₂ layer was deposited with low-pressure chemical vapor deposition (Tystar Mini-Tytan), and a 314-nm layer of Si₃N₄ was deposited in the plasma chemical vapor deposition system (Oxford Instruments Plasmalab 100). Then, a layer of electron-beam resist poly(methyl methacrylate) (PMMA) A5 (AllResist gmbh) was spin-coated on the sample at 5000 rpm and 5000 acceleration for 30 s, followed by baking on a hotplate at 180° C for 3 min. The resist was then patterned by exposing it in the electron beam lithography setup (Elionix ELS-F125), with an area dose of electron beam exposure of 1400 μC/cm², at 125 kV and 1 nA. The exposed pattern was developed in 1:3 IPA: MIBK for 60 s, rinsed in IPA for 20 s. The metal mask was then formed by depositing an 8-nm titanium and a 25-nm nickel using the electron beam evaporation system AJA ATC-1800-E and the subsequent lift-off process at 80 C using NMP (1-methyl-2-pyrrolidone). The designed pattern was transferred to the material using a reactive ion etching in the ICP-RIE system (Trion) at 8 mT, 12 sccm SF₆, 150 W RF, and 8 W ICP with the etch rate of ~2 nm/s. Finally, the metal mask is removed by wet etching using piranha solution, three parts of sulfuric (95-98%) acid H₂SO₄ and one part of hydrogen peroxide (30%) (H₂O₂) at room temperature. Electron microscope images of the resulting samples were obtained using a scanning electron microscope (Thermo Fisher Scientific Helios G4).

Exfoliation and transfer. The capping hBN flake, and WS₂ and WSe₂ monolayers were mechanically exfoliated with 3M Scotch tape on a polymer film (Gel-Fim® WF ×4, Gel-Pak, CA) [34]. The heterostructure stack of hBN/WS₂/WSe₂ was then assembled using a dry transfer method as follows. A polydimethylsiloxane (PDMS; SYLGARD™ 184 Silicone Elastomer, Dow, MI) stamp was prepared on a glass slide. Then a solution of polyvinyl alcohol (PVA), glycerol, and water (weight ratio 5:1:100) was drop-cast onto the stamp and dried on a hot plate at 42° C for 15 minutes. Next, the PVA/PDMS stamp was used to sequentially pick up the hBN, WS₂, and WSe₂ flakes at 70 °C, while aligning them with a custom-built setup. The completed stack was placed onto the target waveguide and released at 120° C.

Optical measurements. The fabricated device was tested with a supercontinuum light source NKT Fianium FIU-15 with a tunable VARIA frequency filter to guide light at 620 and 750 nm. The 870 nm channel was tested with a M-squared SOLSTIS Ti:Sapphire laser. Exciton emission was measured using a lab-built confocal microscopy setup with a fixed 532 CW laser excitation. The 4F system and scanning mirror allowed for decoupling of the collection from the excitation. A 100× 0.9 NA objective (Nikon) was used for both excitation and collection, directing light to a spectrometer (Princeton Instruments Acton SP2300) or an avalanche photodiode (APD) (Excelitas SPCM AQRH-14-FC) through a multimode fiber.

Acknowledgements

The authors acknowledge the use of the fabrication facilities and scientific and technical assistance from the Research and Prototype Foundry Core Research Facility at the University of Sydney, being a part of the NCRIS-enabled Australian National Fabrication Facility (ANFF), and the UTS and UNSW facilities, being a part of the ANFF-NSW node. The authors acknowledge Takashi Taniguchi (the National Institute for Materials Science) for providing hBN crystals and John Scott for silicon nitride substrates. This work was performed in part at the Melbourne Centre for Nanofabrication (MCN), the Victorian Node of the ANFF. The authors acknowledge financial support from the Australian Research Council (CE200100010, FT220100053), the Office of Naval Research Global (N62909-22-1-2028). H.R. acknowledges the funding support from the Australian Research Council (DE220101085, DP220102152).

References

1. Lin, H., et al., *Engineering van der Waals Materials for Advanced Metaphotonics*. Chemical reviews, 2022. **122**(19): p. 15204-15355.
2. Xu, H., et al., *Van der Waals Heterostructures for Photoelectric, Memory, and Neural Network Applications*. Small science, 2024. **4**(4): p. n/a.
3. Zhang, Y., et al., *Advanced optical polarizers based on 2D materials*. npj Nanophotonics, 2024. **1**(1): p. 28.
4. Zhang, Q., et al., *Recent progress in emerging two-dimensional organic-inorganic van der Waals heterojunctions*. Chemical Society reviews, 2024. **53**(6): p. 396-3133.
5. Sierra, J.F., et al., *Van der Waals heterostructures for spintronics and opto-spintronics*. Nature nanotechnology, 2021. **16**(8): p. 856-868.
6. Mak, K.F., et al., *Atomically Thin MoS₂: A New Direct-Gap Semiconductor*. Physical review letters, 2010. **105**(13).
7. Splendiani, A., et al., *Emerging Photoluminescence in Monolayer MoS₂*. Nano letters, 2010. **10**(4): p. 1271-1275.
8. Schaibley, J.R., et al., *Valleytronics in 2D materials*. Nature reviews. Materials, 2016. **1**(11): p. 16055.
9. Chernikov, A., et al., *Exciton Binding Energy and Nonhydrogenic Rydberg Series in Monolayer WS₂*. Physical review letters, 2014. **113**(7).
10. Ye, Z., et al., *Probing excitonic dark states in single-layer tungsten disulphide*. Nature (London), 2014. **513**(7517): p. 214-218.
11. Wang, G., et al., *Giant Enhancement of the Optical Second-Harmonic Emission of WSe₂ Monolayers by Laser Excitation at Exciton Resonances*. Physical review letters, 2015. **114**(9).
12. Mak, K.F., et al., *Control of valley polarization in monolayer MoS₂ by optical helicity*. Nature Nanotechnology, 2012. **7**(8): p. 494-498.
13. Bussolotti, F., et al., *Roadmap on finding chiral valleys: screening 2D materials for valleytronics*. Nano Futures, 2018. **2**(3): p. 032001.
14. Bie, Y.-Q., et al., *A MoTe₂-based light-emitting diode and photodetector for silicon photonic integrated circuits*. Nature nanotechnology, 2017. **12**(12): p. 1124-1129.
15. Radisavljevic, B. and A. Kis, *Mobility engineering and a metal-insulator transition in monolayer MoS₂*. Nature materials, 2013. **12**(9): p. 815-820.

16. Kumar Mandal, K., et al., *A photonic integrated chip platform for interlayer exciton valley routing*. Journal of applied physics, 2023. **133**(12).
17. Liu, Y., et al., *Room temperature nanocavity laser with interlayer excitons in 2D heterostructures*. Science advances, 2019. **5**(4): p. eaav4506-eaav4506.
18. Molesky, S., et al., *Inverse design in nanophotonics*. Nature Photonics, 2018. **12**(11): p. 659-670.
19. Su, L., et al., *Nanophotonic Inverse Design with SPINS: Software Architecture and Practical Considerations*. 2019.
20. Piggott, A.Y., et al., *Fabrication-constrained nanophotonic inverse design*. Scientific reports, 2017. **7**(1): p. 1786-7.
21. Lou, B., et al., *Inverse Design of Optical Switch Based on Bilevel Optimization Inspired by Meta-Learning*. ACS photonics, 2023. **10**(6): p. 1806-1812.
22. Jin, C., et al., *Ultrafast dynamics in van der Waals heterostructures*. Nature nanotechnology, 2018. **13**(11): p. 994-1003.
23. Rivera, P., et al., *Interlayer valley excitons in heterobilayers of transition metal dichalcogenides*. Nature nanotechnology, 2018. **13**(11): p. 1004-1015.
24. Wang, K., et al., *Interlayer Coupling in Twisted WSe₂/WS₂ Bilayer Heterostructures Revealed by Optical Spectroscopy*. ACS nano, 2016. **10**(7): p. 6612-6622.
25. Zhu, M., et al., *Exchange between Interlayer and Intralayer Exciton in WSe₂/WS₂ Heterostructure by Interlayer Coupling Engineering*. Nano letters, 2022. **22**(11): p. 4528-4534.
26. Piggott, A.Y., et al., *Inverse design and demonstration of a compact and broadband on-chip wavelength demultiplexer*. Nature photonics, 2015. **9**(6): p. 374-377.
27. Shen, B., et al., *An integrated-nanophotonics polarization beamsplitter with 2.4 × 2.4 μm² footprint*. Nature photonics, 2015. **9**(6): p. 378-382.
28. Li, Z., et al., *Inverse design enables large-scale high-performance meta-optics reshaping virtual reality*. Nature communications, 2022. **13**(1): p. 2409-2409.
29. Zhang, Z., et al., *Folded Digital Meta-Lenses for on-Chip Spectrometer*. Nano letters, 2023. **23**(8): p. 3459-3466.
30. Wierzbowski, J., et al., *Direct exciton emission from atomically thin transition metal dichalcogenide heterostructures near the lifetime limit*. arXiv.org, 2017.
31. Kim, H., et al., *Synthetic WSe₂ monolayers with high photoluminescence quantum yield*. Science advances, 2019. **5**(1): p. eaau4728-eaau4728.
32. Cho, C., et al., *Highly Strain-Tunable Interlayer Excitons in MoS₂/WSe₂ Heterobilayers*. Nano letters, 2021. **21**(9): p. 3956-3964.
33. Pak, S., et al., *Strain-Mediated Interlayer Coupling Effects on the Excitonic Behaviors in an Epitaxially Grown MoS₂/WS₂ van der Waals Heterobilayer*. Nano letters, 2017. **17**(9): p. 5634-5640.
34. Novoselov, K.S., et al., *Electric Field Effect in Atomically Thin Carbon Films*. Science (American Association for the Advancement of Science), 2004. **306**(5696): p. 666-669.